Model selection in fracture mapping from elastostatic data

B. Lecampion *, J. Gunning [1]

CSIRO Petroleum, Melbourne Office, PB 10, Clayton South, Vic. 3169, Australia

Abstract

In this paper, the inverse problem of imaging internally pressurized cracks from elastostatic measurements is investigated with special attention to the question of model choice. The selection of the most probable model from among a finite set of fracture geometry and loading model is carried out using Bayes factors. The modelling error variance is also estimated during the inversion procedure. This Bayesian model selection method also produces a known limit for the resolution of fracture dimensions, which depends on the configuration of the measurements. Both synthetic and real field examples in hydraulic fracture mapping applications are presented.
Crown copyright © 2006 Published by Elsevier Ltd. All rights reserved.

Keywords: Crack detection; Inverse problem; Bayesian model selection; Hydraulic fracturing

1. Introduction

Model choice problems arise in inverse theory when data are analyzed to obtain a quantitative estimation of some properties of a system whose interior characteristics are not well understood. In engineering applications, the data are usually inverted using a particular forward model, which is chosen a priori, and whose validity is not in dispute. This is not always the case: in many instances, aspects of the model may be quite uncertain, such as adequate knowledge of a boundary condition, or the postulated behaviour of a material, etc. Further, the chosen forward model may fit the data but still be inadequate for prediction or extrapolation. In such cases, one may question the usefulness and range of validity of the results obtained by inverse analysis with a single fixed model. Quantitative model selection and hypothesis testing for data analysis have received considerable interest in the statistical and 'softer' science communities (social, medical, etc.) in the last decade. The Bayesian approach to the model selection problem has gained considerable support due to its versatility and solid theoretical basis. Nonetheless, the investigation of model selection in engineering is nearly non-existent with the exception of Beck and Yuen (2004), though some interest has arisen in the geosciences, especially with regard to the problem of modelling heterogeneous media (Malinverno, 2002).

---

* Corresponding author. Tel.: +61 3 9545 8379; fax: +61 3 9545 8380.
  E-mail addresses: Brice.Lecampion@csiro.au (B. Lecampion), James.Gunning@csiro.au (J. Gunning).
[1] Tel.: +61 3 9545 8396; fax: +61 3 9545 8380.

We are interested in the model selection problem arising in the mapping of internally loaded cracks from elastostatic measurements inside or on the boundary of an elastic solid. This particular inverse problem arises in applications such as non-destructive testing in engineering mechanics, and the detection of quasi-static faults or man-made hydraulic fractures in geophysics. We are concerned chiefly with model uncertainties in the parametrization of the crack geometry and loading. Our motivation is related to hydraulic fracturing, a technique routinely used in the petroleum industry to enhance the productivity of reservoir formations. Mapping of the produced fracture is of great importance to oil companies for reservoir management purposes. In practice, monitoring of the quasi-static deformation induced by such cracks is often carried out using high precision tiltmeters: these measure a local, relative, quasi-static change of inclination due to the pressurization and/or propagation of the hydraulic fracture. Typically, a measurement array would consist of *at most* a dozen tiltmeters located either on the earth's surface or in a monitoring borehole (see Fig. 1). Within practical constraints, the array is designed to yield the least ambiguous data for inference of the fracture orientation and geometry. Unfortunately, due to the elliptic character of quasi-static elasticity, the geometric signatures of the fracture are attenuated very quickly as the distance between the measurement location and the fracture increases. In the far-field, the fracture becomes equivalent to a Displacement Discontinuity singularity (i.e. a dislocation dipole), which simplifies the forward modelling, but only fracture orientation and volume can then be estimated (Lecampion et al., 2005). When measurements are located in the near-field, the shape of the fracture has an important effect and the choice of the fracture model (geometry, internal loading) becomes meaningfully inferable.

Several methods have been proposed for the identification of a stress free crack from redundant boundary elastostatic data. In these cases, data are supposed to be available on part or the whole boundary of the solid for a series of associated boundary loads (see Bonnet and Constantinescu, 2005 for a review). The methods of solution range from the minimization of the data misfit with a parametrization of the crack (e.g. mesh characteristic or geometrical parameters) (Chen and Nisitanu, 1993; Stravoulakis and Antes, 1997; Larson et al., 1999 and Weikl et al., 2001 among others) to the use of 'defect indicators' such as the reciprocity gap functional (Andrieux et al., 1999; Ben Abda et al., 1999) and topological sensitivity (Gallego and Rus, 2004). Very few examples with real data have been published to our knowledge, with the exception of Larson et al. (1999). Here, we are interested in a different problem, where the cracks are internally loaded and *few* measurements inside or on the boundary of the solid are available. Further, the loading responsible for the observed data is unknown. And unlike in the case of non-destructive testing, there is no practical freedom to adjust the loading to better resolve the fracture.
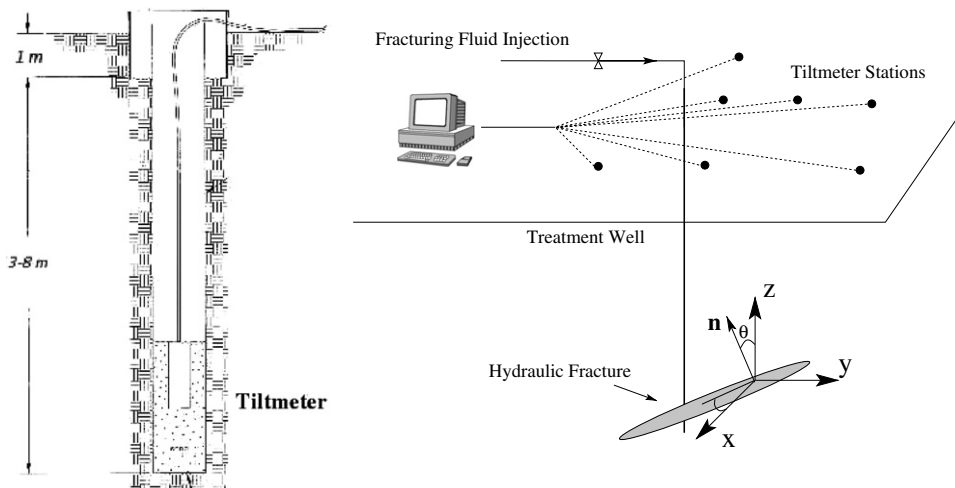

Fig. 1. Set-up of tiltmeter in shallow boreholes (left, After `Appl. Geomechanics Inc.`), and typical layout of a measurement array for fracture monitoring (right).

In petroleum applications, the fracture is located in a rock mass that can be rather inhomogeneous and whose elastic properties are often poorly known. Even when the measurements are known to be located in the near-field region of the fracture, the use of a complete mesh to model the fracture is more or less prohibited by the unknown orientation of the fracture plane, and the limited measurements available. For engineering purposes, it is more pragmatic to use a collection of computationally inexpensive fracture models (radial or elliptical crack, square Displacement Discontinuity, single Displacement Discontinuity singularity, etc.) to analyze the data, although all these models may be *incorrect*. Within this scope, it is natural to investigate the problem of model selection and model uncertainty.

The remainder of this paper is organized as follows. In Section 2 we outline the forward modelling problem, its associated inverse problem, and discuss relevant aspects of a typical measurement set-up. In Section 3 we present a Bayesian model selection procedure. Computational and theoretical aspects are discussed. A synthetic example (Section 4) shows the benefits of such an approach, especially in relation to the far-field/near-field fracture resolution problem. Finally (Section 5), real tiltmeter data from a full scale hydraulic fracturing treatment are also inverted and different possible fracture geometries are tested. Section 6 summarises our conclusions.

2. Problem description

2.1. Type of measurements

The methodology presented in this paper is valid for any type of elastostatic measurements, such as those measured by strain gauges, LVDT (linear variable differential transformer), extensometers etc. The examples presented in this paper focus on tiltmeter data. High precision tiltmeters with a resolution down to a nanoradians are used to measure the small deformation induced by remote hydraulic fractures. These instruments are clamped to the rock formation in boreholes (Fig. 1), and record the change of inclination induced by the fracture at a sampling rate of 5–10 s. The measured tilt angles $w_{1,2}$ (along two orthogonal axis (e_1, e_2) of the instrument) are related to two components of the curl of the quasi-static displacement vector $\boldsymbol{u}$ in the rock mass by

$$w_1 = \frac{\partial u_3}{\partial x_1} - \frac{\partial u_1}{\partial x_3}, \quad w_2 = \frac{\partial u_3}{\partial x_2} - \frac{\partial u_2}{\partial x_3}. \tag{1}$$

Typically, due to practical and cost constraints; only a dozen instruments or so are used in field applications. Fig. 2 shows the two tilts recorded by a tiltmeter during a real hydraulic fracturing treatment. The change of tilt induced by the propagation of the hydraulic fracture can be clearly seen, as well as the beginning of the return of the tilt toward zero after the end of the injection. This return is delayed due to fracture closure and the consolidation effect linked with the diffusion of fracturing fluid in the rock mass.
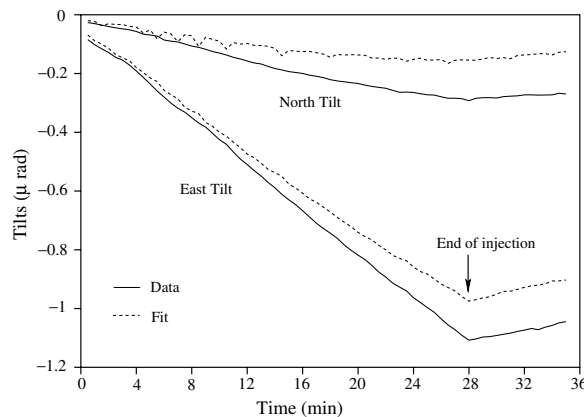

Fig. 2. Field experiment: typical evolution of tilt data during a hydraulic fracturing treatment. The corresponding best fit obtained by sequentially inverting the data with a static fracture model (DD singularity) is also displayed.

The change of tilt between the beginning of the injection and a particular time t, obtained at several points in the medium, provides accurate data for an inverse problem for the fracture geometry. The model used to invert the data are static fracture models, fitted to the total deformation measured since the beginning of the fracturing process. A likely extension of the inverse problem is sequential inversion of the data at a series of times steps during the injection period, for monitoring the growth of the hydraulic fracture.

2.2. The forward and inverse problems

The elastostatic deformation and tilts induced by an internally loaded fracture S is a solution of the following elastostatic boundary value problem in the domain Ω:

$$\begin{aligned} \operatorname{div} \boldsymbol{C} : \varepsilon(\boldsymbol{u}) &= \boldsymbol{0} \quad \text{in } \Omega \setminus S, \\ (\boldsymbol{\sigma} \cdot \boldsymbol{n}) &= p(x) \quad \text{on } S, \end{aligned} \tag{2}$$

where $\boldsymbol{C}$ is the tensor of elastic moduli, $\boldsymbol{u}$ the displacement field, ε the small strain operator $\varepsilon(\boldsymbol{u}) = \frac{1}{2}(\nabla \boldsymbol{u} + \nabla^{\mathrm{T}} \boldsymbol{u})$. and $\boldsymbol{\sigma} = \boldsymbol{C} : \varepsilon(\boldsymbol{u})$ the stress tensor. Additional boundary conditions on the boundary of the solid are needed to complete the elastostatic problem. In this paper, we consider only the case of a pressurized fracture in an infinite domain, such that the additional boundary conditions are vanishing displacement and stress at infinity.

The internal fracture loading $p(x)$ can be related to a displacement jump $[D]$ of the fracture faces. This forward problem can be recast in the framework of eigenstrain theory, so the displacements, stresses and tilts can be obtained by a superposition of Displacements Discontinuity Singularities (see Eshelby, 1957; Mura, 1982; Hills et al., 1996). For example, the displacement in the case of an opening mode fracture in an unbounded medium can be expressed as

$$u_i(\boldsymbol{x}) = \int_S U_{ijk}(\boldsymbol{x}, \boldsymbol{x}') n_j n_k D_n(\boldsymbol{x}') \, \mathrm{d}\boldsymbol{x}'. \tag{3}$$

In our notation, $(U_{ijk} \cdot D_{jk})$ denotes the displacement u_i at $\boldsymbol{x}$ induced by a DD singularity of the form D_{jk} located at $\boldsymbol{x}'$. $(D_{jk} \cdot n_k)$ represents a displacement jump across an element oriented by its unit normal n_k. We define $D_n = D_{ij} n_i n_j$ as the normal component of the displacement jump. Similar integral representations exists for the displacement gradient, stress and tilts. We note that the fundamental kernel U_{ijk} – which is in fact the jk-component of the stress tensor at $\boldsymbol{x}'$ generated by a unit point force along i at $\boldsymbol{x}$ – is regular everywhere except on the fracture ($\boldsymbol{x} = \boldsymbol{x}'$). In the case of fracture monitoring, the instruments are located outside the fracture domain, simplifying the evaluation of the integral in Eq. (3).

The inverse problem consists in finding the fracture dimensions, the orientation $(S, \boldsymbol{n})$ and the opening profile $D_n(\boldsymbol{x}')$ from observations of the tilts w_1, w_2 at $N/2$ different tiltmeter stations in the medium. This data forms an observation vector $\boldsymbol{d}$ of length N.

Before discussing the solution of this ill-posed problem, we recall a recent result for the resolution of fracture dimensions from elastostatic measurements (Lecampion et al., 2005). It can be shown that the details of the fracture shape are attenuated very quickly as the distance between the measurements and the fracture increases: a typical consequence of St. Venant's principle in elasticity. Observations located in the far-field deformation pattern of a pressurized fracture are only sensitive to the volume and orientation of the fracture: in the far-field the fracture is equivalent to a Displacement Discontinuity singularity with an intensity equal to the fracture volume. A severe non-uniqueness for fracture dimensions exists in that case. In the case of near-field measurements, the shape as well as the internal pressure of the fracture start to have a visible effect on the deformation field. The far-field/near-field transition has been estimated using a far-field expansion in terms of the fracture length of a finite fracture solution in a full-space (Lecampion et al., 2005). Far-field monitoring conditions are defined by the region

$$r > \ell(1 + |\cos \beta|),$$

where r is the distance between the measurement and the fracture center, ℓ is the characteristic length of the fracture and β is the angle between the fracture plane and the measurement location. This result is extremely important in practice, as the measurements are often far from the fracture with respect to its length. By

introducing the resolution index $\mathscr{R} = (\ell(1 + |\cos\beta|))/r$, we can distinguish between two kinds of practical cases, near-field ($\mathscr{R} \gtrsim 1$) and far-field ($\mathscr{R} \lesssim 1$).

For far-field fracture mapping, a simple DD singularity model (i.e. $U_{ijk}(\boldsymbol{x}, \boldsymbol{x}')n_j n_k$) with an intensity equal to the fracture volume can be used to robustly invert the data and obtain the fracture volume and orientation. For near-field cases, the dimensions of the fracture may be resolved but the choice of the proper geometrical model becomes crucial. The limited information content in the data and the application of Occam's principle mitigate against the use of a high dimensional model for the fracture geometry. We thus deliberately avoid the use of a discretization (using boundary elements for example) of the integral equation (3) in order to obtain a finite linear inverse problem for the opening at each node for example. It is also obvious that the characteristic length ℓ of the created fracture is not known a priori, so it is difficult to judge by inspection whether the data correspond to the near or far-field regimes. In the following, simple fracture geometries and loading will be used to analyze the data. Such simple parametrizations of the fracture, with analytical expressions for the tilts, enable fast solution of the inverse problem.

With several candidate models, the choice of the best model requires explicit inversions for each model. For a model $\mathscr{M}_k$, the recorded tilt data $\boldsymbol{d}$ can be formally represented as:

$$\boldsymbol{d} = \boldsymbol{g}_k(\boldsymbol{m}_k) + \boldsymbol{\epsilon}_k, \tag{4}$$

where $\boldsymbol{g}_k$ is the model function simulating the tilt. In the case of fracture detection, $\boldsymbol{g}_k$ is a nonlinear function of the parameters $\boldsymbol{m}_k$ of the model $\mathscr{M}_k$. The model parameter vector $\boldsymbol{m}_k$ contains the fracture orientation (with normal $\boldsymbol{n}$ defined by Euler angles), dimensions parameters etc. The noise vector $\boldsymbol{\epsilon}_k$ lumps the experimental and modelling noise for the particular model $\mathscr{M}_k$. This noise process depends on the chosen model (i.e: modelling error) and depends on statistical parameters that must be jointly inverted with the fracture model. For simplicity, we assume that the noise $\boldsymbol{\epsilon}_k$ is Gaussian of zero-mean and variance $\sigma_k^2 : \boldsymbol{\epsilon}_k = \mathscr{N}(0, \sigma_k^2 \boldsymbol{I})$, which implies assumptions of independence and stationarity.

Given a data set $\boldsymbol{d}$ representing the deformation induced by the fracture, we seek to estimate, among a set of pre-supposed models $\mathscr{M}_k, k = 1, 2, \ldots$ the most probable model, along with its corresponding model parameters $\boldsymbol{m}_k$ and model noise variance σ_k^2. To achieve this, we solve an inverse problem for each model and then use a Bayesian criterion to rank the different models.

3. Bayesian model selection

3.1. Bayes factors

The posterior probability of model $\mathscr{M}_k$, after the data have been observed, can be written using Bayes' rule as

$$p(\mathscr{M}_k | \boldsymbol{d}) = \frac{p(\boldsymbol{d} | \mathscr{M}_k) p(\mathscr{M}_k)}{p(\boldsymbol{d})}. \tag{5}$$

The denominator $p(\boldsymbol{d})$ in Eq. (5) denotes the probability that the data have been observed, and is a constant which is taken to normalize the expression as $p(\boldsymbol{d}) = \sum_k p(\boldsymbol{d} | \mathscr{M}_k) p(\mathscr{M}_k)$. Here, $p(\mathscr{M}_k)$ is the prior probability of model $\mathscr{M}_k$ and $p(\boldsymbol{d} | \mathscr{M}_k)$ is the marginal probability of the data (also sometimes denoted the integrated likelihood) for model $\mathscr{M}_k$. This last quantity involves an integral over the entire parameter space for the given model $\mathscr{M}_k$:

$$p(\boldsymbol{d} | \mathscr{M}_k) = \int \int p(\boldsymbol{d} | \boldsymbol{m}_k, \sigma_k) p(\boldsymbol{m}_k, \sigma_k) \, \mathrm{d}\boldsymbol{m}_k \, \mathrm{d}\sigma_k. \tag{6}$$

In expression (6), the conditional probability $p(\boldsymbol{d} | \boldsymbol{m}_k, \sigma_k)$ is the probability that the data $\boldsymbol{d}$ were generated by model $\mathscr{M}_k$ with parameters $\boldsymbol{m}_k, \sigma_k$, and is usually called the Likelihood function for parameter estimation problem. The probability $p(\boldsymbol{m}_k, \sigma_k)$ is the prior probability on the model parameters and model variance for model $\mathscr{M}_k$. We shall refer to $\pi(\boldsymbol{m}_k, \sigma_k | \boldsymbol{d}) = p(\boldsymbol{d} | \boldsymbol{m}_k, \sigma_k) p(\boldsymbol{m}_k, \sigma_k)$ as the Bayesian posterior distribution for model $\mathscr{M}_k$.

To compare two models, we compute the ratio of their posterior probability as in Eq. (5):

$$\frac{p(\mathcal{M}_1|\boldsymbol{d})}{p(\mathcal{M}_2|\boldsymbol{d})} = \underbrace{\left[\frac{p(\boldsymbol{d}|\mathcal{M}_1)}{p(\boldsymbol{d}|\mathcal{M}_2)}\right]}_{B_{12}} \left[\frac{p(\mathcal{M}_1)}{p(\mathcal{M}_2)}\right]. \tag{7}$$

The first factor B_{12} is the so-called Bayes factor: it is the ratio of the marginal probability of the data (6) for the models $\mathcal{M}_1$ and $\mathcal{M}_2$. The second factor is the ratio of the model prior probability, and in many cases will be set to unity, so model 1 and 2 are equiprobable prior choices. The main quantity of interest is thus the Bayes factor B_{12}. As noted in Raftery (1996), when the Bayes factor B_{12} is greater than 10, the data clearly favours the model $\mathcal{M}_1$ over the model $\mathcal{M}_2$. When $0.2 < B_{12} < 5$, both models can be though to consistently reproduce the data. Finally for $B_{12} < 0.1$, the data clearly favour the model $\mathcal{M}_2$ over the model $\mathcal{M}_1$.

In our case the set of models is discrete, so the general solution of the model selection problem can be split into two parts. First, for each model $\mathcal{M}_k$, from the posterior pdf $\pi(\boldsymbol{m}_k, \sigma_k|\boldsymbol{d})$, we estimate the marginal probability $p(\boldsymbol{d}|\mathcal{M}_k)$ of the data using Eq. (6). Second, the full set of Bayes factors are computed in order to rank the different models. The main difficulty is to compute the marginal probability of the data for model $\mathcal{M}_k$, which involves an integration over the entire parameter space in Eq. (6).

3.2. Definition and solution for a given model

In this section, we define all the required probability density functions (pdf) for a given model $\mathcal{M}_k$, but drop the reference to k for clarity. The likelihood is taken as a normal probability function for the error in Eq. (4):

$$p(\boldsymbol{d}|\boldsymbol{m}, \sigma) = \frac{1}{(2\pi\sigma^2)^{N/2}} \exp\left[-\frac{1}{2\sigma^2}(\boldsymbol{d} - \boldsymbol{g}(\boldsymbol{m}))^{\mathrm{T}}(\boldsymbol{d} - \boldsymbol{g}(\boldsymbol{m}))\right]. \tag{8}$$

We assume that the prior on the model parameters $p(\boldsymbol{m}, \sigma)$ is independent of the prior on the noise variance, so

$$p(\boldsymbol{m}, \sigma) = p(\boldsymbol{m})p(\sigma) \tag{9}$$

and we choose normal forms for the prior on the model parameters $\boldsymbol{m}$:

$$p(\boldsymbol{m}) = \frac{1}{(2\pi)^{h/2}|\boldsymbol{C}_p|^{1/2}} \exp\left[-\frac{1}{2}(\boldsymbol{m}_p - \boldsymbol{m})^{\mathrm{T}}\boldsymbol{C}_p^{-1}(\boldsymbol{m}_p - \boldsymbol{m})\right]. \tag{10}$$

Here $\boldsymbol{m}_p$ is a vector of prior means for the h parameters of model $\mathcal{M}$, and $\boldsymbol{C}_p$ is the corresponding prior covariance matrix with its determinant noted as $|\boldsymbol{C}_p|$. As the error variance should be a positive scale number, we re-parametrize and use $\alpha = \log\sigma$ as the unknown, where $\alpha \in (-\infty, +\infty)$. We choose an uniform distribution for α, which can be interpreted as a 'flat prior on the order of magnitude of σ'. Taking into account the Jacobian of the transformation we obtain $p(\sigma) = 1/\sigma$ (or equivalently $p(\log\sigma) = 1$). Such a prior is usually referred to as Jeffrey's prior in the literature. It may also be more formally derived from scale invariance arguments (see Denison et al., 2002; Scales and Tenorio, 2001), and is well known to exhibit a non-integrable character. The latter is not an issue in our application, as we form an approximate posterior pdf based on a Gaussian approximation around the maximum a posteriori point (see below), which is a well defined pdf. Introducing the vector $\boldsymbol{z} = (\boldsymbol{m}, \alpha)$ of dimension $h + 1$ as the total unknowns, we write the prior $p(\boldsymbol{m}, \alpha) = p(\boldsymbol{m}) = p(\boldsymbol{z})$ and likelihood $p(\boldsymbol{d}|\boldsymbol{m}, \sigma) = p(\boldsymbol{d}|\boldsymbol{z})$.

It remains only to characterize the posterior pdf $\pi(\boldsymbol{m}, \sigma|\boldsymbol{d}) = \pi(\boldsymbol{z}|\boldsymbol{d}) = p(\boldsymbol{d}|\boldsymbol{z})p(\boldsymbol{m})p(\sigma)$ and compute the marginal probability of the data for the given model (6). The chief quantities of interest in the posterior pdf are the mode location (most likely solution), and the dispersion about this point (parameter uncertainties). We note that the use of Monte-Carlo Markov Chain (MCMC) methods to characterize the posterior has become very popular in the last few decades, mainly due to the advance of computational power (Gilks et al., 1996). We do not pursue this possibility, since respectable approximations to the quantities of interest can be obtained with cheaper means.

The mode is located using standard Newton-based optimization techniques. For characterization of the dispersion, we approximate the posterior by a normal multivariate pdf centered on the mode. These approximations are much cheaper than MCMC methods, and have proved stable and accurate for our problem.

The model marginal probability (6) in general requires a high dimensional integration, and is usually numerically intractable. Several methods can be used in order to obtain an approximation to the integral: we refer to Kass and Raftery (1995), Raftery (1996) for a complete discussion. We use analytical integrations based on the normal approximation at the mode (the Laplace estimate), which provide good approximations.

Finding the mode $\tilde{z}$ of the posterior $\pi(z|d)$ is equivalent to finding the minimum of the functional $\mathscr{J}(z) = -\log \pi(z|d)$, which takes here the particular form (from Eqs. (8)–(10)):

$$\begin{aligned} &\mathscr{J}(z = (m, \alpha)) \\ &= \frac{N+h}{2}\log(2\pi) + \frac{1}{2}\log|C_p| + N\alpha + \frac{1}{2}\exp(-2\alpha)(d - g(m))^{\mathrm{T}}(d - g(m)) + \frac{1}{2}(m_p - m)^{\mathrm{T}}C_p^{-1}(m_p - m). \end{aligned}$$

(11)

The minimization on α can be performed analytically, to produce an nonlinear least squares problem for m, which can be solved using either Newton or Marquardt methods. We use a quasi-Newton algorithm (BFGS with a Wolfe line search), which is computationally very efficient, but only converges to a local minima. In order to globalize the algorithm, the optimization is re-started from several randomly drawn initial guesses away from the first minima obtained (Nocedal and Wright, 2002).

The second step consists in approximating the posterior pdf around its mode. A quadratic approximation of the functional $\mathscr{J}(z) = -\log \pi(z|d)$ around its minimum $\tilde{z}$ is consistent with a normal approximation of the posterior probability $\pi(z|d)$ around $\tilde{z}$:

$$\pi(m, \sigma|d) = \pi(z|d) \approx \pi(\tilde{z}|d)\exp\left(-\frac{1}{2}(z - \tilde{z})^{\mathrm{T}}\widetilde{C}^{-1}(z - \tilde{z})\right),$$

(12)

where $\widetilde{C}$ is the posterior covariance matrix at $\tilde{z}$. This covariance matrix is the inverse of the Hessian of the functional $\mathscr{J}(z)$ at the minimum $\tilde{z}$. The form of the covariance matrix is derived in Appendix A for the case where the noise parameter is unknown. For our particular problem, and the models used, the functional $\mathscr{J}(z)$ has proved to be relatively smooth and convex, and the normal approximation of the posterior generally appears very good in salient cross-sections of the log-posterior (see Fig. 3).

Computationally, once a minimum $\tilde{z}$ of $\mathscr{J}(z)$ has been obtained, the covariance matrix $\widetilde{C}$ can be estimated in order to approximate the posterior. The approximation (12) enables an estimation of the marginal probability of the model defined by Eq. (6):

$$p(d|\mathscr{M}) \approx \pi(\tilde{z}|d)(2\pi)^{(h+1)/2}|\widetilde{C}|^{1/2}.$$

(13)

Other approximations have been suggested in order to estimate the marginal probability $p(\mathscr{M}|d)$. One of the most popular is the Bayesian Information Criterion (BIC), which originates in a simplification of (13) obtained by assuming that the covariance matrix $\widetilde{C}$ is diagonal. This somewhat crude approximation does not require the computation of the covariance matrix, and seems to be adequate to compare different models when the data is numerous (see Raftery, 1995 for a complete discussion). We prefer the more exact approximation of Eq. (13) for computing the Bayes factors.

3.2.1. Effect of prior

The significance and use of prior probability distributions has been a topic of much debate in Bayesian estimation (Scales and Tenorio, 2001; Denison et al., 2002). We do not intend to discuss this topic in detail, but some aspects of the notion of 'uninformative priors' warrant discussion in relation to model selection.

Consider the case that, for a particular model, no a priori information on parameter m_i is available. From Eq. (10), this lack of a priori information might be interpreted as requiring a large variance $(C_p)_{ii}$. Taking $(C_p)_{ii}^{1/2}$ as a very large multiple of the prior value $(m_p)_i$ ensures that the prior does not have an effect on the mode of the posterior probability. This is easily seen from the form of the functional $\mathscr{J}$ Eq. (11) as $(m_i - (m_p)_i)^2/(C_p)_{ii}$ becomes negligible for very large $(C_p)_{ii}$. Such large values also do not modify the estimated covariance matrix $\widetilde{C}$ at the mode (see Appendix A). However, the prior covariance does directly impact the term $\log|C_p|$ term in Eq. (11), which scales the value $\pi(\tilde{z}|d)$ of the posterior and thus drastically affects the marginal probability of the model $p(d|\mathscr{M})$, as well as any Bayes factor computed from it. Such large non-informative priors will always
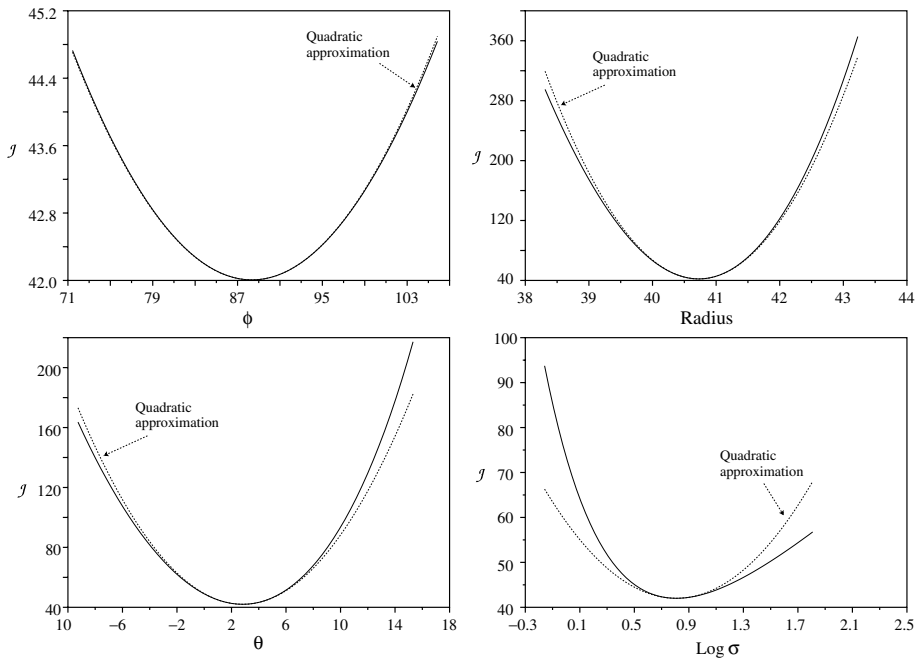
Fig. 3. Cross-section of the cost functional $\mathscr{J} = -\log \pi(z|d)$ and quadratic approximation around the minimum, penny-shaped crack model and synthetic data case.

heavily favour the model with the least number of parameters, when the Bayes factor are computed. This effect is often called the Lindley paradox (see Denison et al., 2002).

Hence, as a rule of thumb, our non-informative priors are formed by taking standard deviations in the prior model parameters value not more than one order of magnitude greater than the prior mean. This ensures that the effect of the prior is minimal in the estimation of the posterior mode, but also that the Lindley paradox has little effect on the estimation of the relative marginal model probabilities. In general, understanding of the physics at the basis of the model provides a sound basis for choosing prior values and variances. We take the prior covariance matrix C_p to be diagonal; since the fracture orientation is related to the initial stress, while the length is related to the injected volume, there is no a priori reason to correlate these parameters in the prior.

4. Synthetic example

4.1. Modelling

We have simulated tilt data due to a penny-shaped crack under constant internal pressure in a full-space for different values of the fracture radius and internal pressure, spanning both far-field and near-field measurement conditions. The simulated data corresponds to the propagation of a penny-shaped (e.g. radial) hydraulic fracture in the so-called *toughness dominated* regime of propagation (Detournay, 2004). In this regime, the propagation of the hydraulic fracture, located in a full space, is self-similar, and the pressure inside the fracture is homogeneous. The evolution of the fracture radius R and dimensionless pressure p/E' are given by power laws of time:

$$R(\tau) = \overline{L}_k \gamma_{ko} \tau^{2/5}, \quad \frac{p(\tau)}{E'} = \bar{\epsilon}_k \Pi_{ko} \tau^{-1/5}, \tag{14}$$

where γ_{ko} and Π_{ko} are constants (Detournay, 2004). The dimensionless time is defined as $\tau = \frac{t}{t_c}$ and the characteristic time t_c is related to the injection rate Q_o, plane strain Young's Modulus E', fracture toughness K' and

fracturing fluid viscosity μ' : $t_c = ((\mu'^{1/5}Q_o^3E'^{13})/K'^{18})^{1/2}$. The characteristic length scale $\bar{L}_k$ and dimensionless number $\bar{\epsilon}_k$ are given by $\bar{L}_k = (E'^3 Q_o \mu')/(K'^4)$ and $\bar{\epsilon}_k = (K'^6/(E'^5 Q_o \mu'))^{1/2}$ respectively. In this example, we have used $\bar{L}_k = 160$, $\bar{\epsilon}_k = 10^{-3}$. The measurements consists of 13 tiltmeter stations (26 tilt data) located in a distributed array approximately 75 m above the center of the fracture. A number of data sets corresponding to increasing fracture radius have been generated. The orientation of the fracture remains constant with a dip θ of 5° and an azimuth of 80° with respect to true North. A Gaussian noise component of standard deviation $\sigma_{input} = 0.8\mu$ radians is added to the tilt data vectors prior to the inversion.

In this synthetic case, the knowledge of the 'true' length of the fracture as well as the distance between the measurements and the fracture dictates if a particular data set corresponds to the far-field or near-field regime. In the case of a penny-shaped crack, the characteristic length scale ℓ is equal to twice the fracture radius. For each data set corresponding to a given value of fracture radius and internal pressure, we can compute the corresponding value of the resolution index $\mathscr{R}$ indicating far or near field conditions. For each value of $\mathscr{R}$, we perform the requisite model selection calculations. Three different models are thought to be able to explain the data (Table 2).

- $\mathscr{M}_1$, a Displacement Discontinuity singularity (fundamental kernel). This model has three parameters: fracture volume V and orientation (dip θ and azimuth ϕ), $\boldsymbol{m} = (\phi, \theta, V)$.
- $\mathscr{M}_2$, a penny-shaped crack of radius R under constant internal pressure $\varepsilon = p_o/E'$, this is the correct model, $\boldsymbol{m} = (\phi, \theta, R, \varepsilon)$.
- $\mathscr{M}_3$, a Square Displacement Discontinuity (DD) panel of half-length a and opening δ : $\boldsymbol{m} = (\phi, \theta, a, \delta)$.

The different elastic solutions in an infinite medium for these models are known in analytical form and are respectively given by Love (1927), Sneddon (1946) or Green (1948), and Rongved (1957) for the fundamental kernel, penny-shaped crack and rectangular DD models.

The same prior information on fracture orientation is taken for all models (see Table 1). The prior on the length-scales or volume are taken un-informative with a standard deviation about one order of magnitude greater than the prior mean value.

4.2. Results

Fig. 4 shows the best fit of the tilt at one measurement location obtained with the different models for all the data sets. Similar fits are visible at all measurement points. The penny-shaped and square DD models both reproduce the data very well for any values of the resolution index simulated. The fit obtained with the DD singularity model deteriorates for $\mathscr{R} > 1$, i.e. when the measurements become "near-field". Similar conclusions can be drawn from the estimated fracture volume obtained by the different models (Fig. 5). In far-field conditions ($\mathscr{R} < 1$), all three models estimate the true fracture volume perfectly, but for near-field conditions ($\mathscr{R} > 1$), the DD singularity model clearly misestimates the fracture volume. Nonetheless, the estimation of the fracture orientation is recovered well by all three models in the near and far-field cases.

Table 1
Table of priors used for the different models (synthetic example)

Models					
		θ (°)	ϕ (°)	V (m³)	
Normal DD sing.	Prior	0	85	10	
$\mathscr{M}_1$	Prior std. deviation	15	15	100	
		θ (°)	ϕ (°)	R (m)	$\varepsilon = p_o/E'$ (10^{-3} –)
Penny-shaped	Prior	0	85	10	0.5
$\mathscr{M}_2$	Prior std. deviation	15	15	100	10
		θ (°)	ϕ (°)	a (m)	δ (10^{-3} m)
Square DD	Prior	0	85	10	1
$\mathscr{M}_3$	Prior std. deviation	15	15	100	100

Table 2
Forward models used and their corresponding parameters

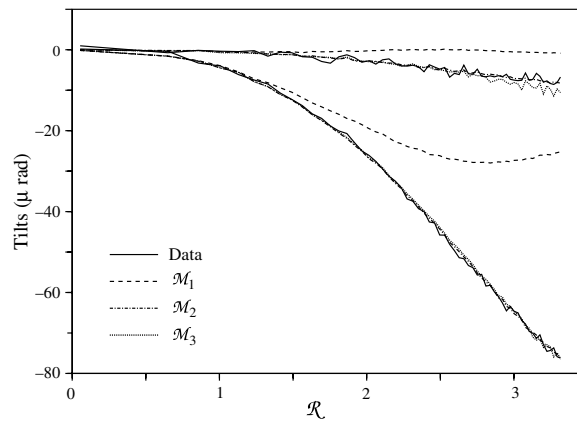| $\mathcal{M}_1$: DD singularity	Volume V	Azimuth–Dip ϕ–θ	
$\mathcal{M}_2$: penny-shaped	Radius R	Dimensionless pressure $\epsilon = p_o/E'$	Azimuth–Dip ϕ–θ
$\mathcal{M}_3$: square DD	Half-length a	DD opening δ	Azimuth–Dip ϕ–θ
$\mathcal{M}_4$: rectangular DD	Half-lengths a and b	DD opening δ	Azimuth–Dip ϕ–θ
$\mathcal{M}_5$: DDS norm and shear	Volume V	Azimuth–Dip ϕ–θ	Shear intensity, orientation and location I, ϕ_s, θ_s, ψ_s and X_s

Fig. 4. Evolution of the fit (2 axis of tilt, station 11) with respect to the resolution index $\mathcal{R}$ for the different models (synthetic example).
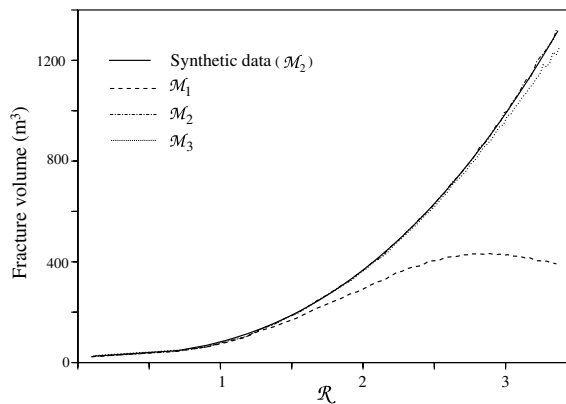

Fig. 5. Volume estimated by the different models versus resolution index (synthetic example).

It is interesting to consider the fracture radius and internal pressure estimated by inverting the data using the penny-shaped model (the 'correct' model). For small value of the resolution index, the estimation of fracture radius and internal pressure are clearly wrong (Fig. 6). The results of the inversion also show, via the posterior covariance matrix $\widetilde{C}$, a complete correlation of the two variables. Only for near-field data ($\mathcal{R} > 1$) are the correct values obtained accurately.
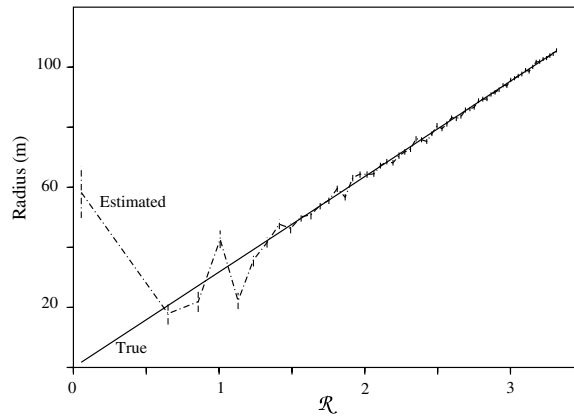
Fig. 6. True and estimated radius versus resolution index for the penny-shaped model (synthetic example).

Figs. 7 and 8 show the evolution of the Bayes factors and estimated model noise standard deviation as the resolution index increases. Interestingly, in the far-field cases ($\mathscr{R} < 1$), the data favours either the DD singularity or square DD model over the penny-shaped, since B_{21} and B_{31} are around 10^{-2}. However, it is difficult to discriminate between the DD singularity and square DD model. In the same regime ($\mathscr{R} < 1$), the identified noise standard deviations are similar for all three models, and close to the value of noise input on the simulated data ($\sigma_{\text{input}} = 0.8\mu$ radians). This indicates, in the far-field, consistency between all the models and the data.

For near-field conditions ($\mathscr{R} > 1$), B_{21} and B_{31} are largely positive (Fig. 7). The Bayes factor B_{23} between the penny-shaped and square DD models does not increase as fast as B_{21}, but still rises quickly above 10^3. In the near-field, as expected, the penny-shaped model is the most probable, followed by the square DD and finally the DD singularity model. Further, the estimated noise standard deviation for the correct model (penny-shaped crack) remains in the same order of magnitude as the input noise ($\sigma_{\text{input}} = 0.8\mu$ radians), while the estimated noise is appreciably larger for both the DD singularity and square DD models as soon as $\mathscr{R} > 1$ (Fig. 8).

It is important to note that conclusions regarding the most suitable model could not have been drawn from the quality of the fit to the data alone (Fig. 4). If it is possible to eliminate for large resolution index the DD singularity model from the lowest quality of the fit, it is impossible to chose between the penny-shaped and square DD model as both produce a similar response. The Bayes factors are required to objectively rank these competing models.
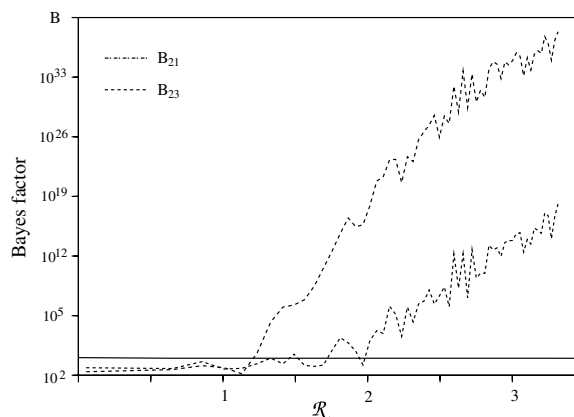

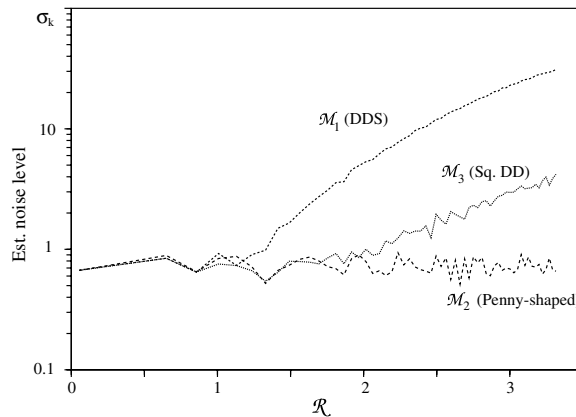Fig. 7. Bayes factor versus resolution index (synthetic example).

Fig. 8. Evolution of the estimated noise standard deviation with the resolution index for the different models (synthetic example).

5. A field example

5.1. Configuration

We examine now measured tilt data obtained during a full-scale hydraulic fracturing experiment performed in October 2002 by CSIRO Petroleum at a mine located in New South Wales, Australia. The rock surrounding the experiment is a hard, quartz monzonite porphyry orebody with an estimated Young's modulus of 50 GPa. A set of sub-vertical natural fractures (dip 85°, azimuth 130°) exist in the zone of the hydraulic fracturing treatment. Over-coring stress measurements performed in the area indicated a stress field with near-vertical minimum principal stresses. The induced hydraulic fracture is thus expected to propagate sub-horizontally (i.e. perpendicular to the minimum in situ stress).

The fracture was driven by the injection of 10 m^3 water over a 30 min period. The injection is localised in a zone – isolated by inflatable packers – of a borehole drilled downward from a small underground gallery located 500 m underground. The data was logged by an array of 13 tiltmeters positioned in two horizontal galleries about 75 m above the fracture initiation point. Each tiltmeter was placed in a 2–3 m hole bored in the tunnel floor. The influence of the tunnel (free surface) on the tilt response has been investigated numerically and has been found to be negligible (less than 1% difference between the tilts obtained). This can be explained by the distance of the tiltmeter from the free surface (around 2 m) and the large distance between the depth where the fracture was initiated (around 75 m down the level where the apparatus were located) compared to the size of the tunnel (6 m diameter). The deformation pattern induced by the pressurized cracks 'radiates' around the tunnel and the 'scattering' effect is minimal. These tests justify the use of forward models assuming an infinite isotropic homogeneous medium (Fig. 9).

Five different full-space fracture models have been investigated (see Tables 2 and 3). Three of them are the previously described models: normal DD singularity, penny-shaped crack and square DD. Two additional models were also tested: a rectangular DD, as well as a model combining a normal mode DD singularity with a shear mode DD singularity. The effect of shear was added in order to take into account any eventual shear deformation that could occur due to slip of the natural fractures surrounding the induced fracture. In all cases, the fracture models are assumed to be centered on the injection point, except for the model combining a normal and shear DD singularity; the shear fundamental DD is allowed to sit anywhere in the medium, as shear is likely to occur on natural fracture surfaces, out of the hydraulic fracture plane. The prior information for all model parameters is shown in Table 3. The prior standard deviation on fracture dimensions is taken relatively loose, reflecting prior ignorance, but knowledge of the state of regional stresses at the site has enabled us to introduce a slightly stronger prior on the fracture orientation parameters. Note that the value of the fracture azimuth ϕ is presented here with respect to magnetic North.
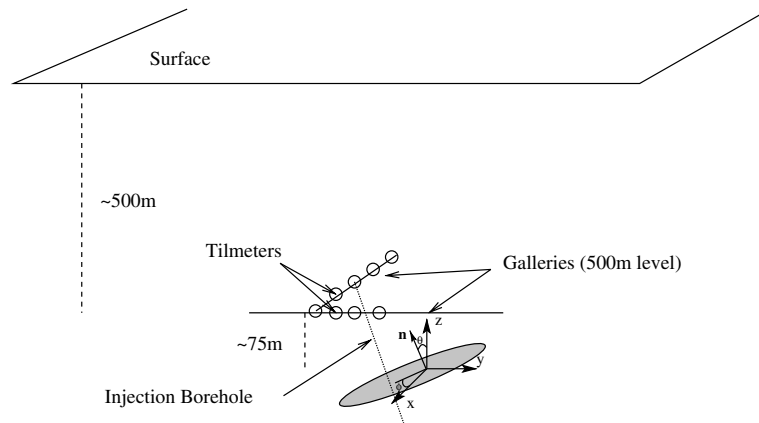
Fig. 9. Sketch (not to scale) of the configuration of the field example. The tiltmeters are located in galleries on the 500 m depth level, approximately on a plane 75 m above the created fracture.

5.2. Results and discussion

Inversions for the different models were carried out with several data sets, corresponding to the total tilt response at increasing time (every minute) during the injection period as well as shortly after the pump was shut-in. The results for the different data sets are presented using their time elapsed from the beginning of the injection as a reference. Tables 4 and 5 summarise the fracture azimuth and dip obtained by the different models with the corresponding standard deviation estimated from the covariance matrix $\widetilde{C}$. These estimations are consistent between models. The a priori value of fracture azimuth is recovered, indicating that the data are uninformative with respect to azimuth. The estimated fracture dip is more refined (lower standard deviation), but there is a larger discrepancy between models. Nonetheless, the fracture is always estimated as sub-horizontal.

The fracture volume estimated by the different models is shown in Fig. 10 (see Table 7 for estimated value and standard deviation at selected time). The results are in good agreement with the injected volume and the loss of fluid (leak-off) in the formation estimated from downhole pressure records. It is interesting to note that the fracture volume is very similar for all models, especially the DD singularities and penny-shaped crack. The finite DD panels (square and rectangular) yield a slightly higher value. The length scales obtained for the finite models are always highly correlated, with no particular trend with regard to fracture growth (Table 6).

Table 3
Table of priors for the different models (Field example)

Models					
		θ (°)	ϕ (°)	V (m³)	
Normal DD sing.	Prior	0	310	10	
$\mathcal{M}_1$	Prior std. deviation	15	20	100	
		θ (°)	ϕ (°)	R (m)	p_o/E' (10^{-3}−)
Penny-shaped	Prior	0	310	30	1
$\mathcal{M}_2$	Prior std. deviation	15	20	100	30
		θ (°)	ϕ (°)	a/b (m)	δ (10^{-3} m)
Square/rectangular DD	Prior	0	310	30	1
$\mathcal{M}_3/\mathcal{M}_4$	Prior std. deviation	15	20	100	30
		Euler angles	I (m³)	Location (x,y,z)	
Shear DD sing.	Prior	0	1	$X_{\text{injection}}$	$+\mathcal{M}_1$ prior
$\mathcal{M}_5$	Prior std. deviation	60	20	50	for normal mode

Table 4
Fracture azimuth (in degrees) estimated by the different models (field example)

Time (min)	DDS		Penny		Square DD		Rectangular DD		Shear + Norm. DDS	
	ϕ	σ_ϕ	ϕ	σ_ϕ	ϕ	σ_ϕ	ϕ	σ_ϕ	ϕ	σ_ϕ
5	131.7	19.64	129.7	19.96	143.0	17.6	120.3	18.9	130.3	6.1
10	133.3	19.45	129.9	19.92	128.3	15.4	123.5	19.0	129.9	5.1
15	133.3	19.25	128.0	19.96	137.5	17.3	158.9	8.41	129.9	4.2
20	131.9	18.89	129.9	19.91	124.7	13.5	158.1	8.86	130.3	3.2
25	132.3	18.85	126.8	19.86	137.4	14.6	132.5	15.9	130.1	2.8
30	131.4	18.60	128.2	19.85	128.2	13.3	132.1	16.7	130.1	2.4
35	129.9	18.31	130.9	19.79	130.6	13.5	91.22	6.59	130.3	2.2

Table 5
Fracture dip (in degrees) estimated by the different models (field example)

Time (min)	DDS		Penny		Square DD		Rectangular DD		Shear + Norm. DDS	
	θ	σ_θ	θ	σ_θ	θ	σ_θ	θ	σ_θ	θ	σ_θ
5	4.7	6.0	0.31	0.83	10.0	5.13	4.12	6.61	−4.99	0.17
10	5.0	5.1	0.422	1.53	9.65	4.52	9.87	7.39	−4.40	0.10
15	5.9	5.1	0.351	1.52	9.61	4.48	15.7	5.12	−4.31	0.10
20	7.7	5.4	1.044	2.17	12.7	4.84	14.6	5.32	−4.58	0.15
25	7.4	5.1	1.40	3.90	12.4	4.11	13.2	5.13	−3.65	0.10
30	8.4	5.3	1.540	5.20	14.0	4.53	15.7	5.50	−3.84	0.11
35	10.2	5.7	2.337	5.99	14.5	4.67	0.44	6.10	−4.24	0.14

Table 6
Fracture dimensions for the square DD model ($\mathcal{M}_3$), with posterior standard deviation and correlation of the identified values (field example)

Time (min)	Half-length		Opening		Correlation
	a (m)	σ_a	δ (mm)	σ_δ	$\rho_{a\delta} = \widetilde{C}_{a\delta}/\sqrt{\sigma_a \sigma_\delta}$
5	53.84	10.5	0.109	0.037	−0.95
10	59.44	8.4	0.168	0.042	−0.94
15	49.62	9.98	0.327	0.118	−0.97
20	62.65	8.30	0.280	0.071	−0.93
25	59.21	7.47	0.373	0.089	−0.93
30	60.60	7.81	0.374	0.095	−0.94
35	62.83	7.83	0.342	0.085	−0.93

Combined with the consistency of the estimated fracture volume, this suggests that the data correspond to a case of far-field conditions during all the injection period.

The different fits obtained are all of the same quality. In Fig. 11, tilt vectors (representing the horizontal component of the displacement curl) are displayed for all tiltmeter stations for the data collected after 20 min of injection. Observe that the fit for two models (DD singularity and rectangular DD) present many similarities. The same applies to the other models. Another view of the fit is presented in Fig. 12, where the observed and computed tilt components at a given station are displayed versus time. The discrepancy between data and estimated results for the different models is illuminated by comparing the corresponding estimated noise standard deviations σ in Fig. 13. The models $\mathcal{M}_1, \mathcal{M}_2, \mathcal{M}_5$ have similar values of σ at all time, but these are larger than the two other models. The noise standard deviation increases linearly for all models during the injection (Fig. 13), so we may reasonably infer that the modelling error becomes larger as the fracture growth. This is probably due to the simplifying assumption of homogeneity in the medium.

Table 8 shows the Bayes factors at different times for all models, taking the normal DD singularity model ($\mathcal{M}_1$) as a reference for comparison. It is clear that model $\mathcal{M}_5$ can be ruled out immediately. Despite a similar fit for the data, the value of the Bayes factor B_{15} is always very large in comparison to other models. This
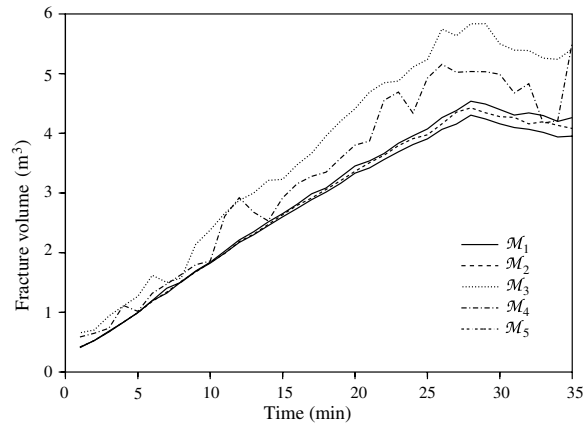
Fig. 10. Estimated fracture volume by the different models versus time (field case).

Table 7
Fracture volume (in cubic meters) estimated by the different models (field example)

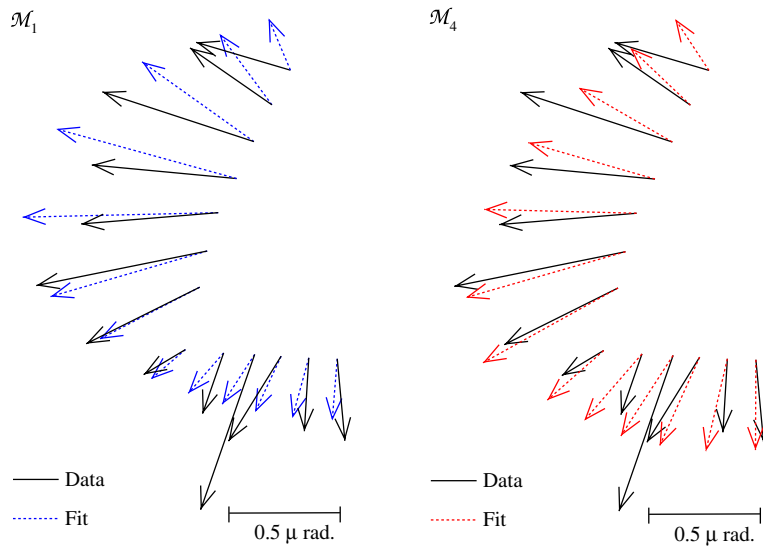| Time (min)	DDS		Penny		Square DD		Rectangular DD		Shear + Norm. DDS	
	V	σ_V	V	σ_V	V	σ_V	V	σ_V	V	σ_V
5	0.99	0.10	0.99	10.0	1.26	0.33	1.01	0.10	0.99	0.25
10	1.84	0.16	1.83	16.2	2.38	0.34	1.85	0.01	1.82	0.20
15	2.65	0.24	2.63	16.1	3.22	0.63	2.91	5.87	2.60	0.21
20	3.45	0.33	3.36	17.6	4.41	0.48	3.80	20.9	3.33	0.32
25	4.07	0.37	3.97	13.8	5.23	0.52	4.92	2.29	3.90	0.26
30	4.39	0.41	4.27	18.6	5.49	0.56	4.98	0.01	4.15	0.29
35	4.26	0.43	4.08	21.2	5.41	0.53	5.52	9.78	3.95	0.36

Fig. 11. Plan view of the tilt vectors fit after 20 min of injection (field case), DD singularity ($\mathcal{M}_1$, left) and rectangular DD ($\mathcal{M}_4$, right) model.

particular model has the largest number of parameters ($h = 10$), yet does not yield a better fit to the data, as the modelling error variance is similar to the other models. All the others Bayes factor are much lower, but still
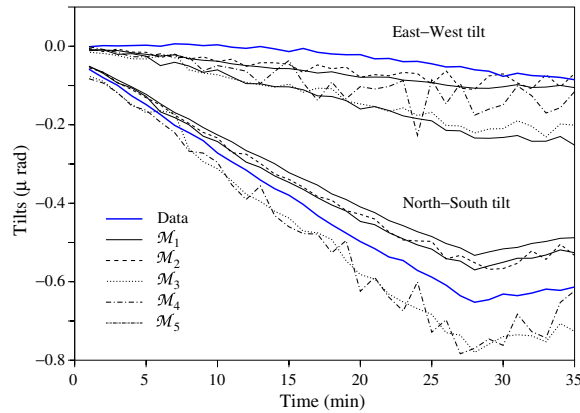
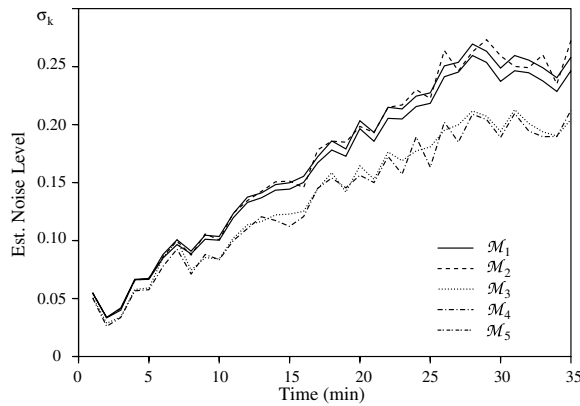Fig. 12. Tilt fit versus time at station 11 (field case).

Fig. 13. Estimated noise standard deviation of the different models versus time (field case).

Table 8
Evolution of Bayes factors (field example)

Time (min)	B_{12} DDS/penny	B_{13} DDS/square DD	B_{14} DDS/rectangular DD	B_{15} DDS/shear + Norm DDS
5	164.90	27.9	13.4	4.86×10^{30}
10	101.77	6.89	6.92	10^{21}
15	156.30	6.90	5.45	10^{19}
20	194.37	6.64	2.98	10^{13}
25	110.12	5.39	2.31	10^{9}
30	107.80	4.18	4.6	10^{8}
35	123.28	5.21	279.4	10^{8}

larger than one, indicating a preference for the simple normal DD singularity model. Notably, the Bayes factor B_{12} (normal DD singularity: penny-shaped model) is always around 100 for all data sets. This implies that the DD singularity model is the most probable among the candidates, for all times. However, the Bayes factor for the square and rectangular DD decreases to a value where both the DD singularity or square/rectangular DD are nearly equi-probable (a Bayes factor under 5 indicates no real preference between two models). This might indicate that, at large time, the fracture may be large enough to create approximate near-field conditions. Observations of fracture length obtained from intersections of the fracture with monitoring boreholes indicate a maximum fracture length of 80 m. The ratio between the distance of the measurements from the

fracture ($\approx$80 m) and the fracture length is therefore at most unity, which means that at large time, the conditions are close to the far-field/near-field limit for the resolution of length scales. Unfortunately, the estimation of the length scales of the finite DD models are strongly correlated and therefore untrustworthy (see Table 6). We conclude that for this particular field-case, far-field mapping conditions were always applicable, so the normal DD singularity model remains the best choice.

6. Conclusions

In this paper an objective method of selecting the most probable model from among a set of fracture geometry and loading models has been described in relation to the imaging of internally loaded cracks from elastostatic data. The model choice is based on Bayes factors computed using the Laplace approximation at the most-probable inversion parameters. The introduction of the noise standard deviation as an unknown in the inversion facilitates testing of the model chosen to analyze the data: the estimated value of the noise must be comparable to the measurement error for a model to be plausible.

A synthetic example demonstrates the advantage of this approach when no definitive models can be a-priori chosen to analyze the recorded data. The far-field/near-field limit of resolution of fracture dimensions has been recovered. In near-field cases, the correct model has been identified from the value of the Bayes factor. For far-field cases, a simple DD singularity (i.e. dislocation dipole) is invariably the most probable model. For an actual field data set, the analysis indicated strongly that the hydraulic fracture did not grow long enough for the near-field effects of the fracture geometry to be meaningfully inferable. Nevertheless, the model choice formalism applied to this actual field data demonstrates well the versatility of the Bayesian model selection method.

In future applications, more complex geometries and fracture propagation models could be tested within the same model selection framework. We also believe that the methodology demonstrated in this paper should be widely applicable to engineering problems involving uncertainty in modelling decisions.

Acknowledgements

Appendix A. A posterior covariance matrix

The quadratic approximation of the functional $\mathscr{J}(\boldsymbol{z} = (\boldsymbol{m}, \alpha)) = -\log \pi(\boldsymbol{z}|\boldsymbol{d})$ around its minimum $\tilde{\boldsymbol{z}}$ (where the gradient vanishes) is

$$\mathscr{J}(\boldsymbol{z} = (\boldsymbol{m}, \alpha)) \approx \mathscr{J}(\tilde{\boldsymbol{z}}) + \frac{1}{2}(\boldsymbol{z} - \tilde{\boldsymbol{z}})^{\mathrm{T}} \widetilde{\boldsymbol{H}} (\boldsymbol{z} - \tilde{\boldsymbol{z}}). \tag{A.1}$$

From this last equation (A.1) and the usual form of the normal probability distribution (12), the Hessian $\widetilde{\boldsymbol{H}}$ is clearly the inverse of the covariance matrix $\widetilde{\boldsymbol{C}}^{-1}$:

$$\pi(\boldsymbol{z}|\boldsymbol{d}) = \exp(-\mathscr{J}(\boldsymbol{z})) \approx \underbrace{\exp(-\mathscr{J}(\tilde{\boldsymbol{z}}))}_{\pi(\tilde{\boldsymbol{z}}|\boldsymbol{d})} \underbrace{\exp\left(-\frac{1}{2}(\boldsymbol{z} - \tilde{\boldsymbol{z}})^{\mathrm{T}} \widetilde{\boldsymbol{H}} (\boldsymbol{z} - \tilde{\boldsymbol{z}})\right)}_{\exp\left(-\frac{1}{2}(z-\tilde{z})^{\mathrm{T}} \widetilde{\boldsymbol{C}}^{-1}(z-\tilde{z})\right)}.$$

The model function $\boldsymbol{g}(\boldsymbol{m})$ is a vector simulating the data vector $\boldsymbol{d}$ (length N). We define the sensitivity matrix, or Jacobian $\boldsymbol{X}$ of dimensions ($N \times h$) as

$$X_{ij} = \frac{\partial g_i(\boldsymbol{m})}{\partial m_j}.$$

From Eq. (11), we obtain

$$H_{ij} = \frac{\partial^2 \mathcal{J}}{\partial m_i m_j} = \exp(-2\alpha)(\boldsymbol{X}^{\mathrm{T}}\boldsymbol{X})_{ij} + (\boldsymbol{C}_p^{-1})_{ij}, \quad i, j = 1, \ldots, h,$$

$$H_{i,h+1} = H_{h+1,i} = \frac{\partial^2 \mathcal{J}}{\partial \alpha m_i} = -2\exp(-2\alpha) \sum_{j=1,N} \boldsymbol{X}_{ij}^{\mathrm{T}}(d_j - g_j(\boldsymbol{m})), \quad i = 1, \ldots, h,$$

$$H_{h+1,h+1} = \frac{\partial^2 \mathcal{J}}{\partial \alpha^2} = 2\exp(-2\alpha) \sum_{j=1,N} (d_j - g_j(\boldsymbol{m}))(d_j - g_j(\boldsymbol{m})),$$

where we have implicitly neglected the second order derivatives of the model function $g(\boldsymbol{m}) \frac{\partial^2 g_i}{\partial m_i m_j}$. This classical 'small-residuals' style approximation is reasonable close to the minimum point (see Fig. 3).

References

Andrieux, A., Ben Abda, A., Bui, H.D., 1999. Reciprocity principle and crack identification. Inverse Problems 15, 59–65.

Beck, J.L., Yuen, K., 2004. Model selection using response measurements: Bayesian probabilistic approach. J. Eng. Mech. ASCE 130 (2), 192–203.

Ben Abda, A., Ben Ameur, H., Jaoua, M., 1999. Identification of 2d cracks by elastic boundary measurements. Inverse Problems 15, 67–77.

Bonnet, M., Constantinescu, A., 2005. Inverse problems in elasticity. Inverse Problems 21, R1–R50.

Chen, D.H., Nisitanu, H., 1993. Detection of a crack by body force method. Eng. Fracture Mech. 45 (5), 671–685.

Denison, D.G.T., Holmes, C.C., Mallick, B.K., Smith, A.F.M., 2002. Bayesian Methods for Non-Linear Classification and Regression. Wiley & Sons.

Detournay, E., 2004. Propagation regimes of fluid-driven fractures in impermeable rocks. Int. J. Geomech. 4 (1), 1–11.

Eshelby, J.D., 1957. The determination of the elastic field of an ellipsoidal inclusion and related problems. Proc. Roy. Soc. Ser. A 241, 376–396.

Gallego, R., Rus, G., 2004. Identification of cracks and cavities using the topological sensitivity boundary integral equation. Comput. Mech. 33, 154–163.

Gilks, W.R., Richardson, S., Spiegelhalter, D.J., 1996. Markov Chain Monte Carlo in Practice. Chapman & Hall.

Green, A.E., 1948. On Boussinesq's problem and penny-shaped cracks. Proc. Cambridge Phil. Soc. 45 (2), 251–257.

Hills, D.A., Kelly, P.A., Dai, D.N., Korsunsky, A.M., 1996. Solution of Crack Problems: The Distributed Dislocation Technique. Kluwer Academic Publishers.

Kass, R.E., Raftery, A.E., 1995. Bayes factors. J. Am. Statist. Soc. 90 (430), 773–795.

Larson, M.C., Arthur Verges, M., Keat, W.D., 1999. Nondestructive identification of three-dimensional embedded cracks in finite bodies by inversion of surface displacements. Eng. Fracture Mech. 63, 611–629.

Lecampion, B., Jeffrey, R., Detournay, E., 2005. Resolving the geometry of hydraulic fractures from tilt measurements. Pure Appl. Geophys. 162, 2433–2452.

Love, A.E.H., 1927. A Treatise on the Mathematical Theory of Elasticity. Dover.

Malinverno, A., 2002. Parsimonious Bayesian Markov chain Monte Carlo inversion in a nonlinear geophysical problem. Geophys. J. Int. 151, 675–688.

Mura, T., 1982. Micromechanics of Defects in Solids. Martinus Nijhoff Publisher.

Nocedal, J., Wright, S.J., 2002. Numerical Optimization. Springer.

Raftery, A., 1995. Bayesian model selection in social research (with discussion). In: Marsden, P.V. (Ed.), Sociological Methodology. Jossey-Bass, San Francisco.

Raftery, A., 1996. Hypothesis testing and model selection. In: Markov Chain Monte Carlo in Practice. Chapman & Hall, pp. 163–187.

Rongved, L., 1957. Dislocation over a bounded plane area in an infinite solid. ASME J. Appl. Mech. 24, 252–254.

Scales, J.A., Tenorio, L., 2001. Prior information and uncertainty in inverse problems. Geophysics 66 (20), 389–397.

Sneddon, I.N., 1946. The distribution of stress in the neighbourhood of a crack in an elastic solid. Proc. Roy. Soc. Ser. A 187 (1009), 229–260.

Stravoulakis, G.E., Antes, H., 1997. Nondestructive elastostatic identification of unilateral cracks through BEM and neural networks. Comput. Mech. 20, 439–451.

Weikl, W., Andra, H., Schnack, E., 2001. An alternating iterative algorithm for the reconstruction of internal cracks in a three-dimensional solid body. Inverse Problems 17, 1957–1975.